When rainfall trapped in fluid inclusion restores the relief of an orogen: Insights from the Cenozoic Himalayas

Raphaël Melis, G. Mahéo, V. Gardien, P. Jame, E. Bonjour, B. Bhandari, A. Pêcher

When rainfall trapped in fluid inclusion restores the relief of an orogen: Insights from the Cenozoic Himalayas

R.Melis[1], G.Mahéo[1], V.Gardien[1], P.Jame[2], E.Bonjour[2], B.Bhandari[3], A.Pêcher[4].

[1]Laboratoire de Géologie de Lyon : Terre, Planète et Environnement, CNRS UMR 5276 - Université Claude Bernard Lyon1 - ENS Lyon – Université de Lyon 69622 Villeurbanne, France

[2] Institut des Sciences Analytiques de Lyon (ISA Lyon), UMR 5280, CNRS, Université Claude Bernard Lyon 1, 69622 Villeurbanne, France.

[3] Department of Geology, Tribhuvan University, Kirtipur, Kathmandu, Nepal.

[4] ISTerre, Université Grenoble Alpes, 38000 Grenoble, France.

Corresponding author: Raphaël Melis (r.melis@hotmail.fr)

Keywords:

• Himalaya

• Stable isotope

• Paleoaltimetry

• Fluid inclusions

• Main Central Thrust

• South Tibetan Detachment

• Quartz

• Fluid-rock interaction

• Tectonics

Abstract

The involvement of meteoric water in orogens dynamics through surface processes is well known as for example in the Himalayas where erosion, resulting of the interplay between climate and tectonics shapes the most spectacular landscapes on the planet. But what about more internal and deepest surface fluid infiltration? Here we report analysis of the $\delta^{18}O_{(water)}$ and $\delta D_{(water)}$ of extracted water from fluid inclusions hosted into Cenozoic quartz veins sampled in the core of the Himalayan range, near the Main Central Thrust and the South Tibetan Detachment. Isotopic and microthermometric values suggest a meteoric origin for the fluids trapped in the quartz of syn- to post-kinematic veins formed between 10 to 20 km depth. Moreover, the isotopic compositions obtained in this study on quartz fluid inclusions water collected along a transect across the Himalayan range evolved with the topography in a similar manner than the modern meteoric water. Considering the age of formation of the quartz veins between 18 and 12 Ma, we deduce that the morphology of the Himalayan topographic front was already shaped during the Miocene but located further north.

1. Introduction

The isotopic composition of modern precipitation is governed by Rayleigh fractionation and vary with several parameters such as the distance from shore and latitude, which are primarily controlled by temperature (Craig, 1961; Dansgaard, 1964) and the amount of precipitation, especially in regions affected by monsoonal rainfall (Dansgaard, 1964; Grujic et al., 2018). Atmospheric temperature also varies with elevation, as does the distance between the source of precipitation and the ground. These parameters have effects on the isotopic composition of rainwater in relation to topography as shown in recent studies (Rowley et al., 2001; Poage and Chamberlain, 2001). Consequently, many studies of past climates rely on meteoric water isotopic composition (mostly $\delta^{18}O$ and δD) reconstruction, especially in mountainous areas where the fundamental question of the interaction between relief and climate can be addressed. However, if many models managed to reconstruct theoretical meteoric water composition, measurements are scare and mostly based on carbonates or micas composition using a thermo-dependent fractionation equation (Rowley et al., 2001; Mulch and Chamberlain, 2007). A classical and more direct approach is to measure the isotopic composition of the water trapped in the fluid inclusions (FIs) of minerals. However, this method is prone to errors due to the intermediate steps required to separate and analyze H and O. Indeed, the D/H ratio is determined after reduction of water by Cr to produce H_2 gas (Donnelly et al., 2001; Evans et al., 2008; Menzies et al., 2014). The $\delta^{18}O$ values of the water is calculated using the mass balance equation of (Kishima and Sakai, 1980) after equilibration of H_2O with CO_2 of known composition (Gardien et al., 2016).

Based on this previous work, we propose to use a recent method (Fourel et al., 2020) that allows the simultaneous measurement of $\delta^{18}O$ and δD of very small quantities of fluid (1-15 µl) in order to improve the accuracy and quality of the isotopic data used in paleo altimetry. This study focused on the study of FIs in quartz veins from Central Himalaya, an area where modern isotopic rainwater composition and spatial variation is strongly affected by topography (Balestrini et al., 2014; Bershaw et al., 2012; Garzione et al., 2000a) and where several paleo-altimetry data have already been obtained (e.g. Gébelin et al. 2013).

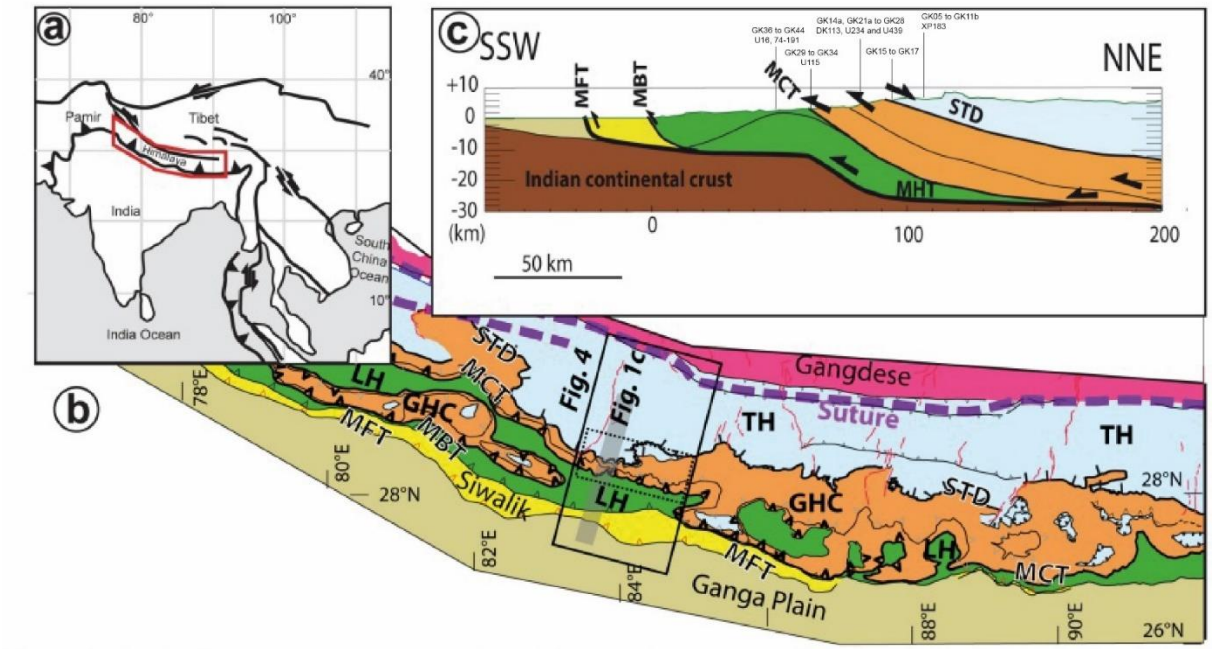

Figure 1 : Geological map and cross-section of the himalayan range (from Leloup et al., 2015). Also shown are the main sampling area and the swath profile location (Fig.4). TH : Tethysian Units ; STD : South Tibetan Detachment ; GHC Greater Himalaya Crystalline ; MCT : Main Central Thrust ; LH : Lesser Himalaya.

2. Geological setting

The Himalayan Range results from the Eocene-age collision between the continental lithospheres of India and southern Asia (Mattauer, 1975). The resulting crustal thickening of the Indian plate is associated with major successive top-to-the-south thrusts, which are, form north to south, the Main Central Thrust (MCT), Main Boundary Thrust (MBT) and still active Main Frontal Thrust (MFT) (Gansser, 1964) (Fig. 1). Seismic data allow to precise their geometry showing that they are developed in the upper crust and are rooted at about 20-30km depth along the Main Himalayan Thrust (MHT) (Zhao et al., 1993) (Fig. 1). All these ductile shear zones (MCT) and faults are parallel to the range strike and delineate the main Himalayan units from south to north (Fig. 1), namely the sub Himalaya bounded by MFT (base) and the MBT (top), Lesser Himalaya (LH) in-between the MBT (base) and the MCT (top). The MCT is also the southern boundary of the Greater Himalayan Crystalline (GHC) which terminates to the north at the South Tibetan Detachment (STD) a north dipping normal shear zone (Burchfiel et al., 1992; Burg et al., 1984). Finally, the STD separates the GHC from the Tethyan Himalaya (TH). The activity of these structures has alternated during the Cenozoic, starting with the motion on the MCT and STD in the early and mid-Miocene, followed by the MBT in the early Miocene and ending with the MFT since the Pliocene (e.g. Yin et al., 2006). Eocene and Oligocene, Eo-Himalayan, deformation is also evidenced in the Tethyan Himalaya (Godin, 2003; Vannay and Hodges, 1996). The main tectonic models proposed to explain the development of the Himalaya orogen include (1) a wedge–like model of a ductile extrusion of the GHC between the MCT and the STD (Burchfiel and Royden, 1985; Burg et al., 1984) ; (2) the southward flow of a lower crust, ductile channel from the Tibetan plateau coupled with focused denudation (e.g. Beaumont et al., 2001; Grujic et al., 2011) ; (3) tectonic wedging (e.g. Webb et al., 2007) or (4) southward-propagating thrust stacking and duplexing (e.g. Carosi et al., 2010; Larson et al., 2015).

3. Sample description

3.1. Quartz veins description

Syn-kinematic, post-foliation and late sub-vertical to vertical quartz veins (Fig. 2) were sampled along the Kali Gandaki river, in Central Nepal, from the STD area down to the MCT as well as a few samples from the TH and LH units (Fig. 1). This dataset was complemented with quartz previously collected by A. Pêcher and P. Le Fort near the Manaslu massif (Table 1). A specific zone, called MCT zone and corresponding to the Lower Greater Himalaya Sequence of Parsons et al. (2016) was distinguished in the upper part of the LH. This zone is comprised between the Chomrong Thrust previously recognized as the MCT (Pêcher, 1978, Vannay & Hodges, 1996; Godin et al., 2001; Iacarrino et al., 2015) and the MCT.

Some quartz grains are associated with aluminous minerals such as muscovite and kyanite in the veins. Rare occurrences of garnet, tourmaline or biotite have also been observed. These veins are similar with hydrothermal quartz veins already described in the Himalaya (Pêcher, 1978; Sauniac and Touret, 1983) as well as in other and various tectonic zones (e.g. Barker et al., 2000; Kawakami et al., 2019; Menzies et al., 2014). Note that such quartz veins are distinct from magmatic veins where plagioclase and K-feldspar are usually also observed. Veins parallel to the host-rock foliation showing evidence of ductile boudinage at the vein's tips are interpreted as syn-kinematic quartz veins (Figs. 2A-F). Among the syn-kinematic veins, we selected mostly those formed by large quartz grains with low and heterogeneous internal deformation (Fig 2. K) for their richness in FIs and the preservation of primary inclusions trapped during the growth of quartz. Highly recrystallized syn-kinematic veins (mylonites), quartz ribbons or quartzite usually used for quartz fabric studies in the GHC (e.g. Larson and Godin, 2009; Leloup et al., 2015) were avoided.

The studied samples are mostly from the same types of quartz veins studied by previous authors (Boullier et al., 1991; Craw, 1990; Derry et al., 2009; Evans et al., 2008; Pecher, 1978; Pêcher, 1979; Sauniac and Touret, 1983).

3.2. Quartz texture and fluid inclusions typology

3.2.1. Quartz texture

Most of the quartz selected for the FIs study do not show significant internal deformation at most bulging recrystallization and undulose extinction) (Figs. 2K) suggesting that no significant quartz recrystallization occurred after veins formation. However, few samples (Figs. 2L) analyzed in this study show greater internal deformation with grain boundary migration indicating high temperature quartz recrystallization (Blumenfeld et al., 1986; Kruhl and Nega, 1996).

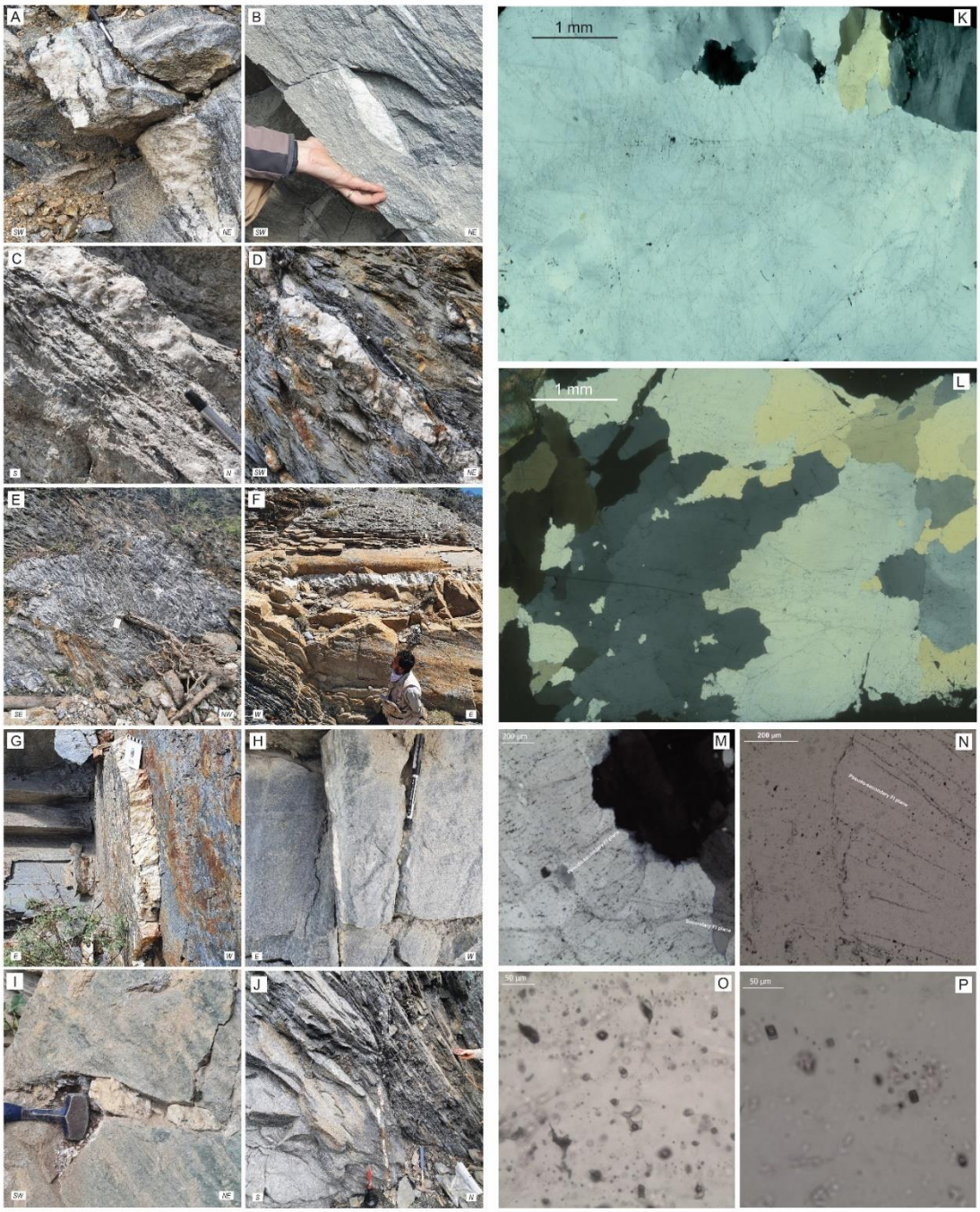

Figure 2 : Pictures illustrating almost all quartz veins sampled allong the Kali Gandaki river, quartz textures and fluid inclusions. (A) (B) (C) and (D) are syn-kinematic quartz veins associated to ductile deformation , respectively GK24, GK26, GK29 and GK37. (E) and (F) are syn-kinematic veins associated to folding, respectively GK34 and GK09a. (G) (H) (I) and (J) are late veins associated to brittle deformation, respectively GK05, GK23, GK16a and GK36. Quartz texture : (K) show slightly deformed large automorphous quartz grain with undulous extinction in sample U439 and (L) showing amoeboid shape grains characteristic of GBM recrystallisation of quartz at high temperature in sample U16. Fluid inclusions observations : (M) (N) and (P) illustrate planes of fluid inclusions up to 20µm that never cross-cut grain boundaries with negative crystal shape which correspond to pseudo-secondary generation (samples XP183 and U16 respectively). On the bottom right corner of (M) there is planes of very small fluid inclusions (< 2 µm) that cross-cut grain boundaries, the secondary generation. (O) illustrate big (up to 40 µm), isolated with «random» shape could correspond to primary generation from sample DK113.

3.2.2. Fluid inclusions typology

Our observations (Fig. 2) show that quartz grains contain several fluid inclusions families. One correspond to rare isolated inclusions in the core of the quartz (Figs. 2O & P) as another generation of more abundant FIs (> 90% of the FIs) is characterized by trails of negative crystal shaped and elliptical inclusions strictly contained inside quartz grain, called fluid inclusion planes (FIP, Figs. 2M,N & P) (Boullier et al., 1991). Finally, a second family of FIP crossing the quartz boundaries healed late cracks (Fig. 2M). These observations are in agreement with previous studies of GHC quartz veins (Boullier et al., 1991; Craw, 1990; Derry et al., 2009; Evans et al., 2008; Pecher, 1978; Pêcher, 1979; Sauniac and Touret, 1983). The homogenization temperature of the FIs obtained by microthermometry range between 300 and 450°C indicating that quartz FIs were formed in this range of temperatures (Boullier et al., 1991; Craw, 1990; Pêcher, 1979; Sauniac and Touret, 1983).

4. Methods

4.1. Fluids extraction

The preparation and the fluid extraction of 32 samples were carried out at the Fluid Inclusions Laboratory of the Geology Laboratory of Lyon. The quartz veins samples were crushed, washed with 3 times diluted nitric acid, rinsed with distilled water, and dried for 48 hours in an oven. Then grains of 500µm to 2 mm diameter were selected by handpicking under binocular to remove altered grains. The quartz grains were placed in quartz tube connected to a vacuum line following the method of Rigaudier et al. (2012). Expansion of fluid held in cavities in the crystals causes the quartz to decrepitate when heated at 600°C. For each sample we extract between 1 to 15 µL of fluid which is then recovered using cryogenic traps.

4.2. Stable isotope analysis

Analyses were performed at the Analytical Sciences Institute in Villeurbanne using an « Off-Axis Integrated Cavity Output Spectrometer » (OA-ICOS) IWA-45EP (Los Gatos Research, Mountain View, California) following the procedure developed in a previous study by Fourel et al., (2020). The water extracted from the FIs is analyzed by repeated injections of 1µl into the spectrometer. The obtained isotopic compositions of water ($\delta D_{(w)}$ and $\delta^{18}O_{(w)}$ values) are averaged and normalized to the standard Los Gatos Research "4C" water sample ($\delta^{18}O_{(w)}$ = -7.-94 ‰, $\delta D_{(w)}$ = -51.6 ‰ and "3C" ($\delta^{18}O_{(w)}$ = -13.39 ‰, $\delta D_{(w)}$ = -97.3 ‰) which were previously calibrated with the IAEA VSMOW2 ($\delta^{18}O_{(w)}$ = 0 ‰, $\delta D_{(w)}$ = 0 ‰). The water analysis of the FIs is bracketed by standard measurements every 7 analysis on average.

5. Results

As a reminder, the fluids contained in all generations of FIs are extracted during the decrepitation of quartz. These values are therefore a mixture composition of primary (very rare), pseudo-secondary (abundant about 90%) and secondary (< 10%) FIs. The composition of $\delta D_{(w)}$ and $\delta^{18}O_{(w)}$ range between -54.83 to -110.94‰ and between -1.74 to -11.09‰, respectively (Table 1). Plotting this values in a δD vs. $\delta^{18}O$ diagram shows that they are located next the modern global meteoric water line ($\delta D = 8\ \delta^{18}O + 10$, Craig, 1961) (Fig. 3)

Table 1

Description of the quartz veins and clefts along the Kali Gandaki and Manaslu section with isotope composition of fluid inclusions. Samples are presented from North to South along the cross sections (Qz = Quartz, Mu = Muscovite, Tourm = Tourmaline, Chl = Chlorite, Ky = Kyanite). Fo: foliation, S1: Schistosity.

Kali Gandaki

Sample	δD_{water} (‰)	$\delta^{18}O_{water}$(‰)	Vein mineralogy	Vein generation	Units	Group	Host rock	Strike ; Dip	Shear sense	Latitude (dd)	Longitude (dd)	Elevation (m)
GK05	-104.43	-10.36	Qz	Late vein	TH	3	Grès / Flysch	Plane : N15 ; 90°	/	28.7679208	83.6984691	2713
GK06	-114.84	-10.16	Qz + Mu	Post-Fo, folded	TH	3	Grès / Flysch	/	/	28.7679208	83.6984691	2713
GK09a	-96.94	-8.40	Qz	Post-S1, folded	TH	3	Quartzite	/	/	28.7668467	83.6981486	2722
GK10	-108.77	-3.83	Qz	Post-Fo	TH	2	Grès / Flysch	Plane : N130 ; 40°SW	/	28.7182426	83.6642024	2620
GK11a	-69.85	-2.94	Qz	Late vein	TH	2	Marbres	/	/	28.697624	83.6249954	2578
GK11b	-69.62	-3.53	Qz+Mu	Post-folding but bouddinaged	TH	2	Marbres	/	/	28.6977212	83.6248912	2569
GK14a	-88.09	-4.31		Post-Fo	GHC	2	Orthogneiss	/	/	28.6587552	83.5909495	2518
GK15	-65.15	-4.59	Qz	Syn-kinematic	STD	2	Marbres	S1 : N116 ; 38°NE	/	28.6658632	83.5850316	2645
GK16a	-69.25	-7.93	Qz+Mu	Post-Fo	STD	3	Marbres	/	/	28.6653542	83.5839612	2692
GK17	-87.68	-8.86	Qz+Tourm	Syn-kinematic	STD	3	Marbres	S1 : N0 ; 20°E	Top to NE	28.6645992	83.5837082	2670
GK21a	-85.64	-7.13	Qz+Chl+Bio	Syn-kinematic	GHC	3	Marbres	/	/	28.6228	83.6282	2310
GK22	-86.48	-8.02	Qz+Bio+Tourm	Syn-kinematic and folded	GHC	3	Marbres	S1 : N90 ; 55°N	/	28.615534	83.6389531	2187
GK23	-75.72	-7.23	Qz	Late vein	GHC	3	Marbres	Plane : N155 ; 90°	/	28.6132522	83.6405166	2158
GK24	-78.07	-7.51	Qz+Bio+Mu+Ky	Syn-kinematic	GHC	3	paragneiss mig	Fo : N135 ; 44°NE	Top to SW	28.5803293	83.6452167	1839
GK28	-88.02	-11.09	Qz+Bio+Mu+Ky	Syn-kinematic	GHC	1	paragneiss	Fo : N110 ; 64°NE	Top to SW	28.570431	83.6389494	1480
GK29	-70.52	-6.68	Qz	Syn-kinematic	MCT	3	paragneiss	S1 : N80 ; 52°NW	Top to SE	28.5462721	83.6450874	1473
GK32	-77.96	-5.93	Qz	Syn-kinematic	MCT	3	Schistes noirs	S1 : N95 ; 47°NE	/	28.533854	83.649191	1412
GK34	-73.37	-6.69	Qz	Syn-kinematic and folded	MCT	3	Schistes noirs	S1 : N95 ; 55°NE	Top to SW	28.528299	83.651037	1394
GK36	-84.95	-9.03	Qz + encaissant	Late vein	LH	1	Schistes noirs	Plane : N130 ; 70°NE	/	28.511074	83.6565014	1299
GK37	-66.32	-3.64	Qz	Syn-kinematic	LH	2	Schistes noirs	S1 : N130 ; 35°NE	/	28.5044524	83.6570361	1268
GK38	-58.48	-6.75	Qz	Post-Fo	LH	3	Grès	/	/	28.485394	83.6476965	1196
GK39	-73.48	-9.48	Qz	Syn-kinematic	LH	1	Grès	Fo : N120 ; 46°NE	/	28.485394	83.6476965	1196
GK42	-54.83	-1.74	Qz	Syn-kinematic	LH	2	Grès	S1 : N12 ; 31°SE	/	28.375834	83.5696446	877
GK43	-68.38	-10.16	Qz	Late vein	LH	1	Quartzite / schiste noir	Plane : N170 ; 30°NE		28.2688587	83.6099669	740
GK44	-71.37	-10.17	Qz	Late vein	LH	1	Quartzite / schiste noir	Plane : N10 ; 24°SW	/	28.2688587	83.6099669	740
Manaslu									/			
XP183	-110.94	-8.75	Qz	Syn-kinematic	TH	3	Schistes noirs	/	/	28.70904	84.59863	4550
DK113	-107.39	-8.25	Qz	Syn-kinematic	GHC	3	Granite folié	Fo : N173 ; 28°NE	/	28.68512	84.47326	4255
U439	-105.47	-7.77	Qz+Mu	Syn-kinematic	GHC	3	Granite	Fo : N120 ; 78°NE	/	28.65437	84.57643	4525
U234	-67.70	-2.10	Qz+Mu	Syn-kinematic	GHC	2	Anatexite	Fo : N110 ; 53°NE	/	28.47393	84.9259	3380
U115	-57.90	-4.91	Qz	Syn-kinematic	MCT	3	Micaschiste à Grt	Fo : N67 ; 35°NE	/	28.33106	84.90709	1400
U16	-60.27	-5.79	Qz	Syn-kinematic	LH	3	Sandstone micaschiste	S1 : N160 ; 50°NE	/	28.082023	84.559429	1570
74-191	-66.01	-5.59	Qz+Mu+Bio	Syn-kinematic	LH	3	Micaschiste	S1 : N90 ; 40°N	/	28.06992	84.65555	540

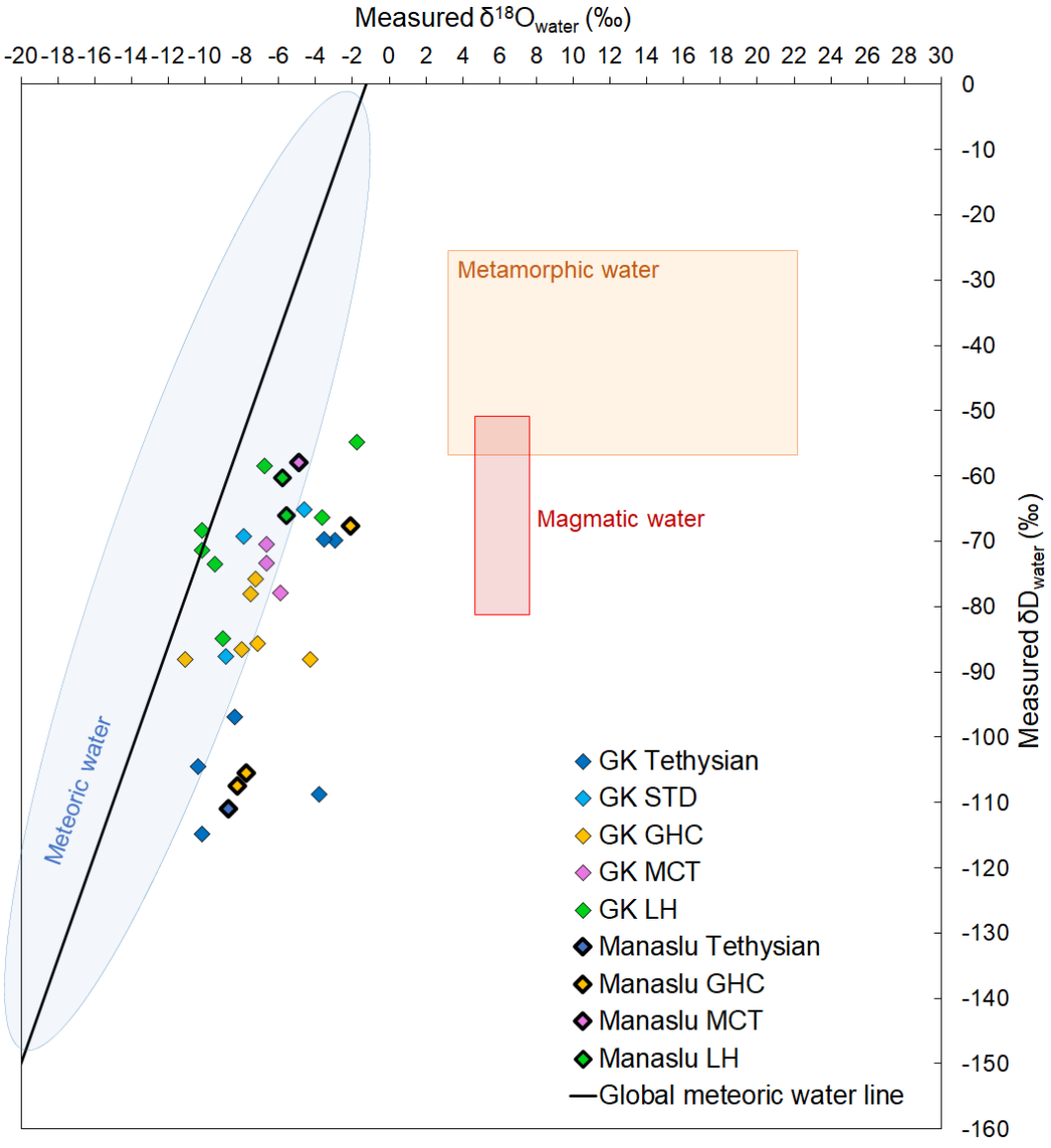

Figure 3 : Plot of $\delta^{18}O_{(w)}$ versus $\delta D_{(w)}$ for fluid inclusions extracted from the different generations of quartz veins. Domains of meteoric, metamorphic and magmatic water are plot.

6. Discussion

6.1. The origin of the fluids

The coupled measurement of the $\delta^{18}O_{(w)}$ and $\delta D_{(w)}$ of an aqueous fluid allow to reconstruct its origin. The water extracted from the quartz FIs (Fig. 3) plots in the global or local (Central Nepal $\delta D = 7.59 \pm 0.14$; $\delta^{18}O = 5.67 \pm 1.9$, Garzione et al., (2000a) and Tibetan plateau ($\delta D = 7.67\ \delta^{18}O + 6.7$, (Bershaw et al., 2012)) meteoric water domain and near the meteoric water lines. This correspondence suggest that the water contained in the quartz is of surface origin. Note that minerals such as muscovite and biotite (e.g. Menzies et al., 2014), tourmaline (e.g. Kawakami et al., 2019) and kyanite (e.g. Barker et al., 2000) are often associated with quartz in hydrothermal veins. Their isotopic composition shows that meteoric fluids may have participated in their formation. However, out of all the samples analyzed, a dozen come out of the meteoric water domain, plotting right of it. This corresponds with a shift of oxygen towards less negative values. Several processes can explain this oxygen drift, such as a mixture between a deep fluid (metamorphic or magmatic) with the surface fluid or a

contamination of the surface water by the surrounding rock or, diffusional oxygen exchange between the host-quartz and water FIs at high temperature (≥ 600°C) (Gilleti and Yung 1984).

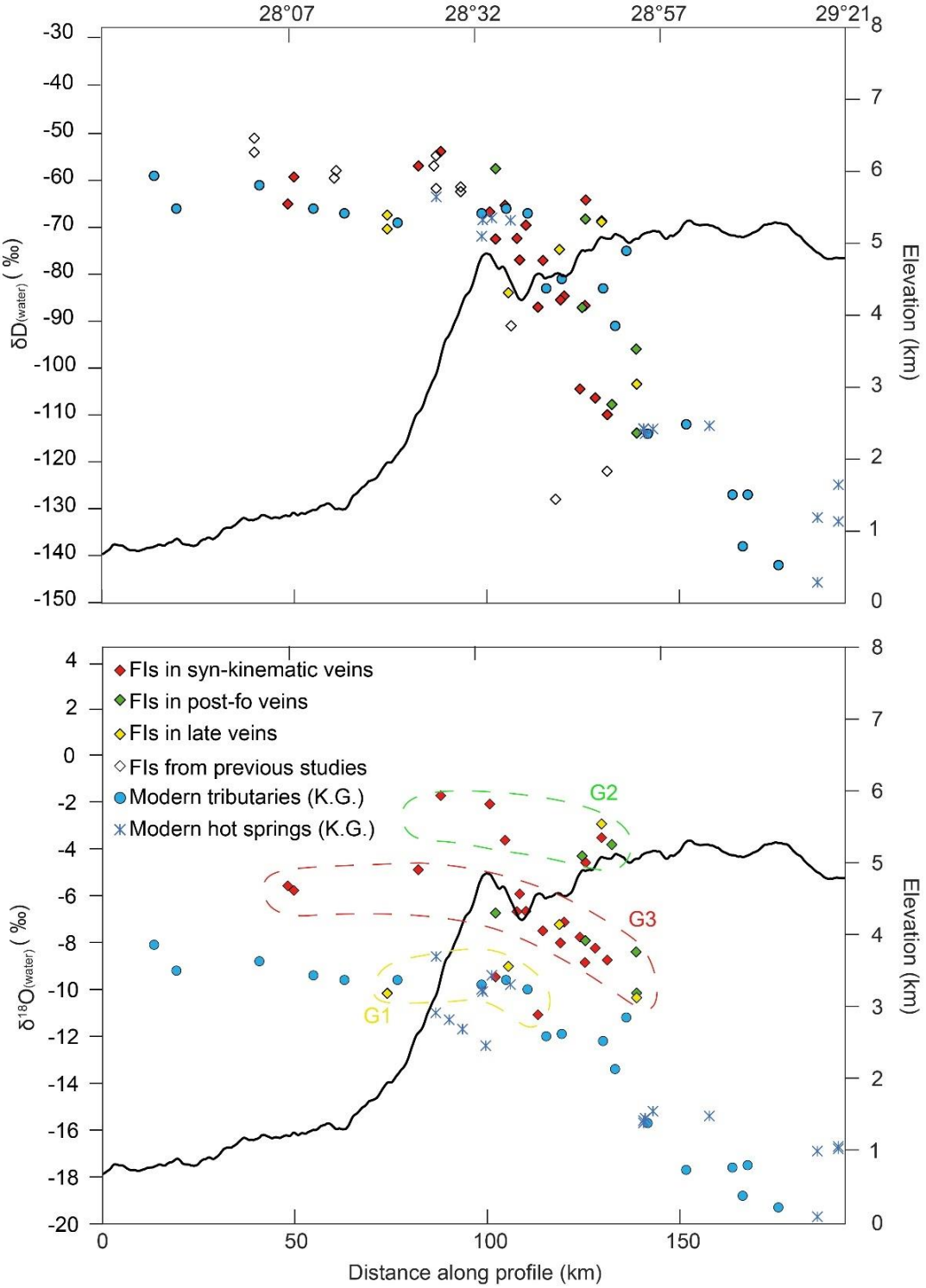

Figure 4 : Variation of the δD(w) and δ18O(w) of modern meteoric water and Miocene fluid inclusions with the himalayan topography. The stable isotope composition of modern tributaries (Garzione et al., 2000), hot springs (Grabczak and Kotarba 1985) and fluid inclusions (this study, France-Lanord et al., 1988 ; Evans et al., 2008), are represented. Thick line of the swath profile correspond to the mean elevation. Dashed color lines correspond to the data enveloppe of each group (G : Group).

Knowledge of the isotopic composition of modern meteoric waters falling on the Himalayan terrain allows to better interpret the data obtained from quartz fluid inclusions. Surface water collected by tributaries of the Kali Gandaki (Garzione et al., 2000b) representing local rainfall averaged with its seasonal variability (ibid.). The isotopic composition of local hot spring water (modern hydrothermal fluids) provides access to potential changes in rainfall water after its transit of several thousand years through the continental crust (Evans et al., 2008; Grabczak and Kotarba, 1985). Figure 4 shows the evolution of the isotopic composition of water in FIs with topography. For a given locality, the $\delta D_{(w)}$ values of the quartz FIs of syn-kinematic and late veins are highly correlated with those of modern water and mean elevation. Note that the $\delta D_{(w)}$ values obtained in this study are similar to values previously obtained on the FIs (Evans et al., 2008). The concordance in spatial distribution of the isotopic composition of modern meteoric water and water released by decrepitation of quartz veins reinforces the meteoric origin of the fluids trapped in the FIs. .

The $\delta^{18}O_{(w)}$ values and spatial distribution of water in quartz FIs is more complex to analyze. Overall three groups can be distinguished (Fig. 4, 5). A first group, plotting on the meteoric water line on Fig. 5, displays the same composition as the modern precipitations and corresponds mainly to quartz in late veins. A second group shows much higher $\delta^{18}O_{(w)}$ values than the modern composition and plots outside of the meteoric water domain (Fig. 5). As previously discussed these compositions most likely reflect contamination by metamorphic or magmatic fluids and / or exchanges with the host rock. A third group that displays $\delta^{18}O_{(w)}$ ratios about 2‰ higher than the modern precipitation and a deuterium excess of -35 +/- 25 ‰ ($d_{excess} = \delta D_{(w)} - 8 * \delta^{18}O_{(w)}$ (Dansgaard, 1964)), shows the same negative correlation with topography as modern precipitations (Fig. 4). Moreover, on a δD vs $\delta^{18}O$ plot these samples defined a line ($R^2 = 0.68$) with a slope of 10.5 in the range of those measured for local meteoric water lines but right-shifted under the global meteoric water line (Fig. 5, see (Putman et al., 2019) for review). All these characteristics (variation with topography, δD vs $\delta^{18}O$ ratio) reinforce the hypothesis of meteoric origin for these fluids. The deviation from the meteoric water line may result from local precipitation conditions such as altitude influencing subcloud evaporation (e.g. Bershaw, 2018) or evaporation at the surface (e.g. in a lake) or a shallow depth (e.g. Jasechko, 2019). Furthermore, as discussed above, the isotopic composition of precipitation can also be altered during infiltration by high-temperature exchange with host rock (Giggenbach, 1992). Finally, deuterium excess can be related to changes in moisture source, relative humidity, temperature and wind speed (e.g. Bershaw, 2018; Jouzel et al., 1982) and may thus record different climatic conditions than modern ones. The negative correlation with topography (Fig. 4) as well as the δD_w vs $\delta^{18}O_w$ relationship (Fig. 5) given by the samples of group 3 most likely reflect a change in moisture source, implying that the meteoric water trapped in the studied FIs record different climatic conditions than today.

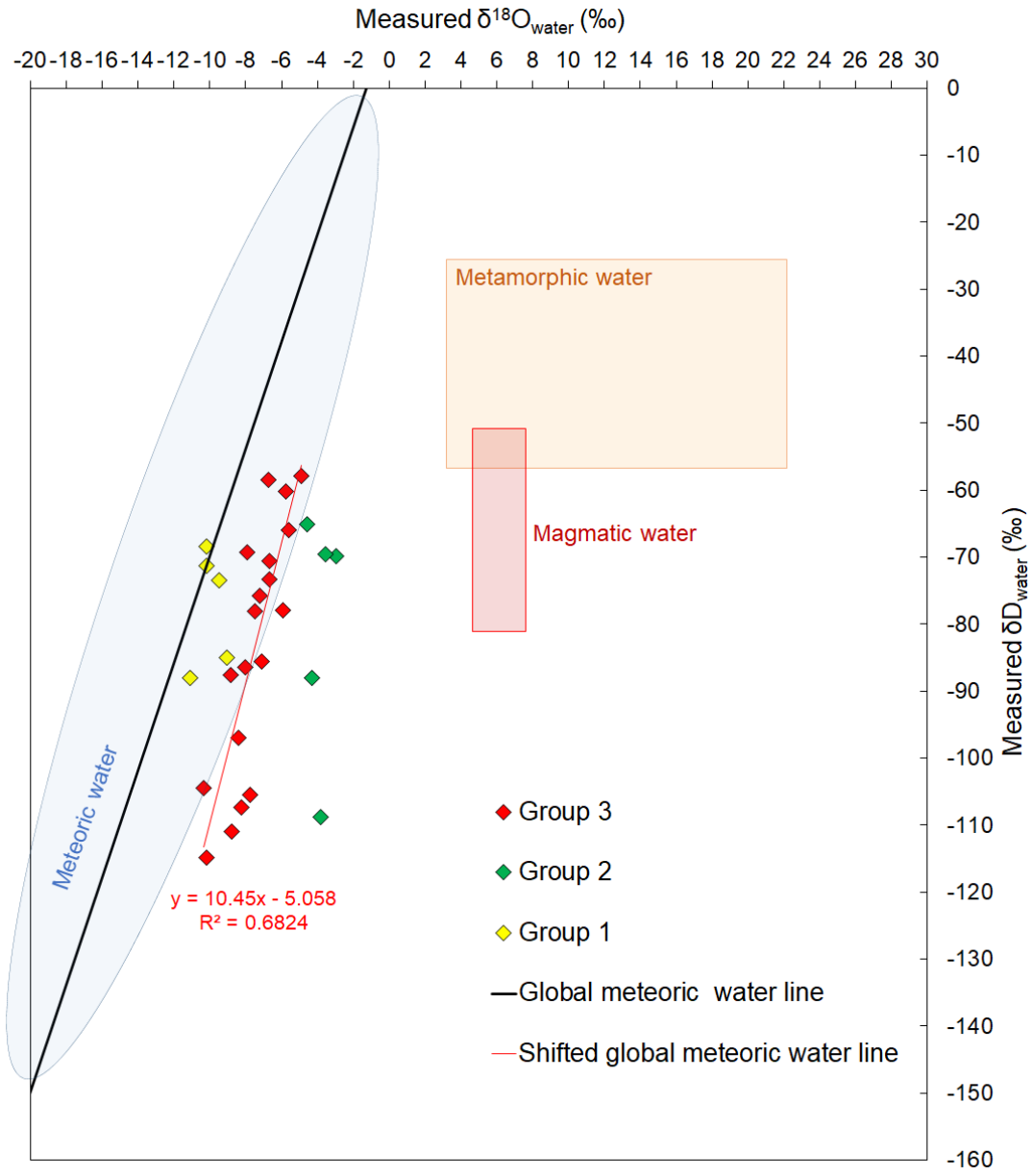

Figure 5 : Plot of δ18O(w) versus δD(w) for fluid inclusions extracted from the different group recognized from Fig. 4 analyses. An apparent meteoric water line shifted of about +2‰ in δ18O from the global meteoric water line can be drawn from the water isotope composition of the fluid inclusions from the group 3.

Until very recently, measurements of the $\delta^{18}O$ of water were not easy and were classically done by analyzing the $\delta^{18}O$ isotopic composition of quartz assuming an isotopic equilibrium between the mineral and the water. However, the calculated $\delta^{18}O_{(w)}$ is always heavier (Evans et al., 2008) than the direct measurement from FIs, which questions the assumption of mineral/fluid isotopic equilibrium.

6.2. Conditions of fluids entrapment

A major question always remains regarding the study of FIs; when was the fluid trapped ? First, the similarity between the composition of the fluids extracted from the quartz and modern precipitation (Fig. 4) may result from diffusion of meteoric water in the exhumed quartz veins at the surface, modifying the initial FIs composition. However, experimental studies of

water diffusion in quartz ruled out diffusion at low temperature (Bakker, 2009). In our case, as the studied quartz is from syn-kinematic veins, secondary FIs can be trapped at any time during quartz deformation and incorporate more and more recent meteoric water. To address this question we can use microstructural and microthermometric data. Microscopic observations show that only few FIs are located at grain boundaries or along late cracks intersecting several quartz grains (Figs., 2M, N, O & P). Moreover, microthermometry on these late FIs gives homogenization temperatures of 150 and 200°C (Boullier et al., 1991). Thus, such FIs are extracted by decrepitation of quartz during a heating step between 100 and 200°C on the vacuum line performed to eliminate the water adsorbed on the surface of the grains. As during this step, the pumping of the line is open, the fluids extracted at low temperature are therefore pumped and very rarely measured.

The main population of FIs in our samples consists of trails of FIs healing former microcracks strictly enclosed in quartz grains. (Figs 2M, N & P). We interpret these FIs as synchronous of the growth of the quartz (Van den Kerkhof and Hein, 2001). The T_h of these FIs range between 300 and 450°C (Boullier et al., 1991; Pêcher, 1978; Pêcher, 1979) for the syn-kinematic quartz veins and around 300°C for the late veins (Craw, 1990; Derry et al., 2009). The sudden and important pressure rises in the vacuum line allows moment and therefore the temperature at which the decrepitation of quartz ("decrepitation temperature" = T_d) occurs to be visualized. The Td is usually higher than the homogenization temperature (T_h) (Van den Kerkhof and Hein, 2001) and can be used as a first order to estimate the trapping temperature of a fluid inclusions generation (Van den Kerkhof and Hein, 2001). Indeed, we observed that the Td of the samples studied were generally between 500 and 600°C. This observation strongly support that the fluids extracted are mainly from FIs formed early during the high temperature growth of quartz and/or early GBM recrystallization. However, a small contribution from late secondary fluids cannot be totally excluded.

6.3. Fluids path and infiltration depth

Although underestimated, the relatively deep introduction of meteoric fluid has been demonstrated at the ductile-fragile transition in orogenic zones (Barker et al., 2000; McCaig et al., 1990). Classically detachment, strike slip, and steep thrust zones are more often invoked as the structures that promote surface (meteoric) fluid infiltration at depth (Gébelin et al., 2013; Menzies et al., 2014; Mulch and Chamberlain, 2007). In contrast, the thrusts responsible for nappe stacking, which are the main cause of crustal thickening, appear to be drains for fluids of metamorphic or magmatic origin, according to some works such as in the Western Alps (Badertscher et al., 2002; Rossi and Rolland, 2014) and in the Himalayas (Boullier et al., 1991; Evans et al., 2008; France-Lanord et al., 1988). However, it should be noted that in these studies the origin of the fluids is often inferred from the sole measurement of $\delta D_{(w)}$ in FIs coupled with a calculation of $\delta^{18}O_{(w)}$ from host $\delta^{18}O_{(quartz)}$.

Coupling the local geothermal gradient of ~35°C/km (Catlos et al., 2018) with the estimated temperature of fluid entrapment at 300-600°C, a formation depth of 8.5 to 17 km can be estimated for the syn-kinematic veins formation. The same depth of 11 to 15 km is obtained with the entrapment pressure FIs of 3-4 kbar (Boullier et al., 1991, Pêcher, 1978; Sauviac & Touret, 1983). In summary, microthermometric data on FIs and microstructural data on quartz are indicative of infiltration and circulation of meteoric water at the brittle-ductile transition zones at 10-20 km depth in the Himalaya (Li et al., 2019).

There are several models to explain the infiltration of fluids into the Himalayan crust. For example: on the STD Gébelin et al., (2017) proposes a vertical infiltration of meteoric fluids from the surface, France-Lanord et al., (1988) invokes a complex model mixing an upward

infiltration of metamorphic fluids from the underlying units of the Lesser Himalayan series or a lateral infiltration from the surface along the deformation zone. In our study we evidence a correlation between the average sampling altitude of the quartz veins and the isotopic composition of their FIs (Fig. 4). Given the age of the quartz veins we suggest that the Himalayan belt elevation effect on precipitation as currently observed (Garzione et al., 2000a; Poage and Chamberlain, 2001; Rowley et al., 2001) already existed during the formation of the syn-kinematic quartz veins, trapping meteoric fluids. This variation in the water isotopic compositions of the FIs is in favor of vertical infiltration of meteoric water from the surface to the trapping depth (Fig. 6). Indeed, a drainage pattern parallel to the large shear structures would give a less wide range of isotopic values corresponding to the elevation of the emerging shear at the surface. Upward infiltration from underlying units along a shear would be dominated by deep fluid isotopic signatures.

This model of vertical infiltration of meteoric fluids has been demonstrated in other mountain zones such as the Mont-Blanc massif (Fontes et al., 1979) in the European Alps, the Pyrenees (Taillefer et al., 2018) and also in the Caledonian range (Barker et al. 2000).

6.4. timing of fluids entrapment

The crucial point is therefore to estimate the age of the quartz formation to infer the age of the FIs. The parallelism between the syn-kinematic ductile quartz veins and the foliation of the metamorphic rocks shows that these veins were formed during the deformation of the host rock. Quartz veins usually formed at the brittle-ductile transition or shallower (e.g. Bons, 2001). Detailed microtectonic and petrologic studies of syn-kinematic veins in the LH, GHC and TH (Pêcher, 1979; Boullier et al., 1991; Sauniac & Touret, 1983) suggest that veins formed at about 300-600°C and are synchronous with the motion of major thrust planes, the MCT and STD in the Himalayas. In the case of quartz that underwent high-T recrystallization (Grain Boundary Migration), trapped FIP are not primary but formed during high-temperature deformation which is believe to be close to quartz growth above 450°C (Boullier et al., 1991, Pêcher, 1978). These deformations are thus also contemporaneous with the GHC deformation during MCT and STD motion. Similar studies on latest quartz veins evidence that FIs where trapped around 300°C (Craw, 1990; Derry et al., 2009).

No geochronological data are available on these syn-kinematic quartz veins, so it is not possible to directly determine when the meteoric fluids were trapped. However, it can be constrained based on the geochronological data available in host-rocks. Along the Kali-Gandaki cross section the thermal peak of metamorphism is dated at 35-32 Ma by U-Pb on monazite and zircon in leucogranite and paragneisses of the GHC series close to the Kalopani shear zone (Godin et al., 2001) and at 22-15 Ma within the STD (Pye et al., 2022). A detailed study of the GHC kyanite-bearing migmatite by Iacarrino et al. (2015), including monazite U-Th-Pb dating, proposed that GHC burial occurred between 43 and 36Ma followed by isobaric heating inducing partial melting. Exhumation of the partially molten crust initiates around 25 Ma and partial melting ends around 18Ma at about 650-700°C (Iaccarino et al., 2015; Parsons et al., 2016).

Cooling of white micas below ~425°C (Harrison et al., 2009) (Ar-Ar method on muscovite) allow determination of the minimum age of ductile deformation between 18 and 12 Ma (Godin et al., 2001; Vannay and Hodges, 1996). Based, on the estimated entrapment temperature of the FIs and the temperature-time-deformation reconstruction of the GHC the formation of the quartz veins can be estimated between the end of ductile deformation at about 18Ma, and ~12 Ma. If one admits that the geochronological data from the host-rocks also apply

to the formation of quartz veins, this implies that the incorporation of fluids within the quartz grains may lasted for a relatively long-time interval.

This in turn may explain the large variability in isotopic composition obtained of the FIs in some areas (Fig. 3). This is particularly the case for samples located in the TH and the STD where Eo- and Neo-Himalayan ductile deformation occurred at 30-35 Ma, 25 Ma and 12 Ma, respectively, before the development of late N-S trending normal faults. However, formation of all the studied quartz veins during a single short event cannot be ruled out.

6.5. Morphologic and climatic implications

The similarity between the isotopic composition of modern precipitation and paleo-precipitations preserved in the FIs of quartz veins (Fig. 4) suggest that during fluids trapping a topographic gradient already existed like the modern one. Our interpretation is consistent with previous studies reconstructing the paleoaltimetry of the Mount-Everest 16 Ma ago (Gébelin et al., 2013) and the Takkhola Grabben ca. 10 Ma ago (Garzione et al., 2000a). Some quartz that we analyzed in this study are in shear zones related to the major thrusts responsible for crustal thickening. Therefore, the variation in the isotopic composition of the FIs along a transect perpendicular to the belt may also be the result of the relative displacement of quartz veins during tectonic processes. However, since 18Ma the GHC has been slowly exhumed as a rigid block (Iaccarino et al., 2015; Parson et al., 2016) by pervasive top-to-the-south shearing in the MCT zone (or LGHS of Parsons et al., 2016)). From the maximum depth of quartz veins formation, exhumation across the LGHS in the Modi Khola valley evidences a relatively homogeneous rate (Parsons et al., 2016). Thus, since 18Ma no significant internal deformation occurred in the GHC and MCT zone. Therefore, we interpret the spatial variation in paleo-precipitation isotopic composition preserved in the FIs as the result of a continuous topographic gradient, located directly above the quartz veins formation zone.

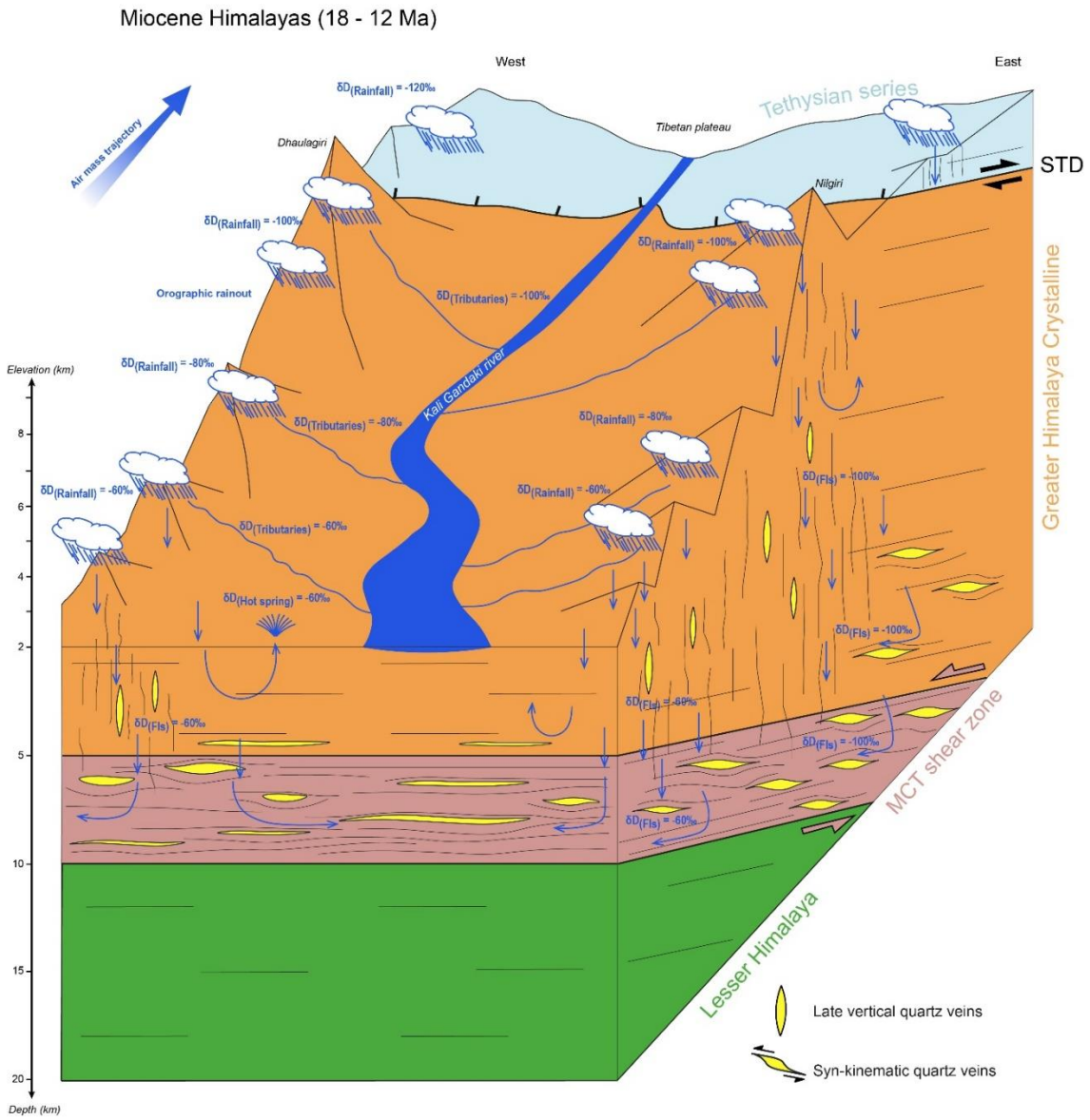

Figure 6 : Conceptual skecth illustrating the meteoric water path through the Greater Himalaya during the Miocene.

To reconstruct the position of this topographic gradient, the location of the quartz veins at the time of their formation must be estimated. When the GHC was extruded during the synchronous motion of the MCT and the STD, this unit moved southward relative to the India-Asia suture zone. Total slip along the STD ranges between a few tens of km to 200 km (e.g. Kellet et al., 2018) since onset of the STD around 25-30Ma (e.g. Kellett et al., 2018; Leloup et al., 2015). An accurate estimate of the formation zone location of the studied quartz veins requires a good knowledge of their formation age. As discussed previously the veins likely formed between 18 and 12 Ma. Thus, the southward motion controlled by the MCT and STD motion must be significantly lower than the total estimated slip along these faults. More-over, slip gives the magnitude of displacement. To constrain the horizontal displacement, the geometry of the fault must be known. The original surface slope of the STD is lower than 10°, as is deep geometry is still controversial (e.g. Kellett et al., 2018; Leloup et al., 2015). In all

cases, displacement magnitude is equal to the horizontal displacement on a horizontal fault or higher. In conclusion, the total displacement of tens of km to 200km along the STD is an upper limit for the location of the studied quartz veins and of the associated topography. On the one hand, assuming either that the veins emplaced near the end of the STD motion at ~12Ma and / or using the lowest estimate of the STD slip magnitude then the topographic front reconstructed in this study should be close to the present day. On the other hand, using the oldest estimated age of the veins formation at ~18 Ma, coupled with an higher STD slip magnitude would imply that the at that time the topographic front was located more than 100km north to the present day position and moved southward relative to the suture zone till the cessation of motion along the STD at about 12Ma.

The Comparison between the reconstituted Miocene paleo-precipitation gradient (12-18 Myr ago) and the modern one allows to discuss the paleoclimatic reconstruction. While the composition and spatial variation of the $\delta D_{(w)}$ of the FIs is similar to that of the modern one the evolution of $\delta^{18}O_{(w)}$ is more complex (Fig. 4). In particular, group 3 data shows the same spatial relationship with topography as modern precipitation but the absolute $\delta^{18}O_{(w)}$ values are shifted by about +2‰ (Fig 4 and 5). This may be related to different climatic conditions between 12 and 18 Ma responsible for variations in the composition of precipitation falling on the Himalayan reliefs. To test this hypothesis, we compare the $\delta^{18}O_{(w)}$ of Miocene precipitation near sea level, in the Himalaya foothill, with modern values. Using $\delta^{18}O_{(carbonates)}$ measured on pedogenic carbonate from the Siwalik foreland paleosols. $\delta^{18}O_{(w)}$ of -5 ‰ and -7 ‰ from 12 to 17 Ma and around -6 ‰ to -11 ‰ at 18 Ma were obtained (see Quade et al., 2013). The 12 to 17 Ma values are close to the modern composition measured in New Delhi (5.8 ‰ ± 0.2 ‰). However, because of the relatively wide range of the Miocene data (about +/- 2.5‰) and uncertainties on the FIs formation age, a climatic control on the observed $\delta^{18}O_{(w)}$ +2‰ shift is difficult to evidence but cannot be ruled out.

Conclusion

Our results present for the first time in the Himalaya a significant data base on the isotopic composition of fluid inclusions in hydrothermal quartz. This data base gives the evolution of the composition of meteoric paleofluids falling on the Himalayas during its formation along a transect that crosscut major tectonic contacts in the mountain range. We used a method newly developed in our lab allowing to analyze simultaneously and directly the δD and the $\delta^{18}O$ isotopic composition of microdroplets (3 to 10 μL) of water contained in FIs. This demonstrate that the composition of meteoric paleofluids falling on the mountain range (Himalaya; Alpes etc…) during its formation can be obtained directly by analyzing the isotopic composition of FIs. These data will provide the necessary constraints on the tectonic and climatic evolution of the region. More precise estimates of the age of quartz vein formation are still needed for a more detailed reconstruction of the Himalayan morphology and to discuss its interaction with tectonic and possibly with climate.

References

Badertscher, N.P., Abart, R., Burkhard, M., McCaig, A., 2002. Fluid flow pathways along the Glarus overthrust derived from stable and Sr-isotope patterns. American Journal of Science 302, 517–547. https://doi.org/10.2475/ajs.302.6.517

Bakker, R.J., 2009. Reequilibration of fluid inclusions: Bulk-diffusion. Lithos 112, 277–288.

Balestrini, R., Polesello, S., Sacchi, E., 2014. Chemistry and isotopic composition of precipitation and surface waters in Khumbu valley (Nepal Himalaya): N dynamics of high elevation basins. Science of the Total Environment 485, 681–692.

Barker, Bennett, Boyce, Fallick, 2000. Retrogression by deep infiltration of meteoric fluids into thrust zones during late-orogenic rapid unroofing: RETROGRESSION BY INFILTRATION OF METEORIC FLUIDS. Journal of Metamorphic Geology 18, 307-318. https://doi.org/10.1046/j.1525-1314.2000.00257.x

Beaumont, C., Jamieson, R.A., Nguyen, M.H., Lee, B., 2001. Himalayan tectonics explained by extrusion of a low-viscosity crustal channel coupled to focused surface denudation. Nature 414, 738–742. https://doi.org/10.1038/414738a

Bershaw, J., 2018. Controls on deuterium excess across Asia. Geosciences 8, 257.

Bershaw, J., Penny, S.M., Garzione, C.N., 2012. Stable isotopes of modern water across the Himalaya and eastern Tibetan Plateau: Implications for estimates of paleoelevation and paleoclimate. Journal of Geophysical Research: Atmospheres 117.

Blumenfeld, P., Mainprice, D., Bouchez, J., 1986. C-slip in quartz from subsolidus deformed granite. Tectonophysics 127, 97–115.

Bons, P.D., 2001. The formation of large quartz veins by rapid ascent of fluids in mobile hydrofractures. Tectonophysics 336, 1–17.

Boullier, A.-M., France-Lanord, C., Dubessy, J., Adamy, J., Champenois, M., 1991. Linked fluid and tectonic evolution in the High Himalaya mountains (Nepal). Contr Mineral Petrol 107, 358–372. https://doi.org/10.1007/BF00325104

Burchfiel, B.C., Royden, L.H., 1985. North-south extension within the convergent Himalayan region. Geology 13, 679–682. https://doi.org/10.1130/0091-7613(1985)13<679:NEWTCH>2.0.CO;2

Burchfiel, B.C., Zhiliang, C., Hodges, K.V., Yuping, L., Royden, L.H., Changrong, D., Jiene, X., 1992. The South Tibetan Detachment System, Himalayan Orogen: Extension Contemporaneous With and Parallel to Shortening in a Collisional Mountain Belt. https://doi.org/10.1130/SPE269-p1

Burg, J.P., Brunel, M., Gapais, D., Chen, G.M., Liu, G.H., 1984. Deformation of leucogranites of the crystalline Main Central Sheet in southern Tibet (China). Journal of Structural Geology 6, 535–542.

Carosi, R., Montomoli, C., Rubatto, D., Visonà, D., 2010. Late Oligocene high-temperature shear zones in the core of the Higher Himalayan Crystallines (Lower Dolpo, western Nepal). Tectonics 29. https://doi.org/10.1029/2008TC002400

Catlos, E.J., Lovera, O.M., Kelly, E.D., Ashley, K.T., Harrison, T.M., Etzel, T., 2018. Modeling High-Resolution Pressure-Temperature Paths Across the Himalayan Main Central Thrust (Central Nepal): Implications for the Dynamics of Collision. Tectonics 37, 2363–2388. https://doi.org/10.1029/2018TC005144

Craig, H., 1961. Isotopic Variations in Meteoric Waters. Science 133, 1702–1703. https://doi.org/10.1126/science.133.3465.1702

Craw, D., 1990. Fluid evolution during uplift of the Annapurna Himal, central Nepal. Lithos 24, 137–150. https://doi.org/10.1016/0024-4937(90)90021-R

Dansgaard, W., 1964. Stable isotopes in precipitation. tellus 16, 436–468.

Derry, L.A., Evans, M.J., Darling, R., France-Lanord, C., 2009. Hydrothermal heat flow near the Main Central Thrust, central Nepal Himalaya. Earth and Planetary Science Letters 286, 101–109. https://doi.org/10.1016/j.epsl.2009.06.036

Donnelly, T., Waldron, S., Tait, A., Dougans, J., Bearhop, S., 2001. Hydrogen isotope analysis of natural abundance and deuterium-enriched waters by reduction over chromium on-line to a dynamic dual inlet isotope-ratio mass spectrometer. Rapid Communications in Mass Spectrometry 15, 1297–1303.

Evans, M.J., Derry, L.A., France-Lanord, C., 2008. Degassing of metamorphic carbon dioxide from the Nepal Himalaya: METAMORPHIC CARBON DIOXIDE. Geochem. Geophys. Geosyst. 9, n/a-n/a. https://doi.org/10.1029/2007GC001796

Fontes, J.Ch., Bortolami, G.C., Zuppi, G.M., 1979. Isotope hydrology of the Mont Blanc Massif. Isotope Hydrology 1978, Hydrologie isotopique du Massif du Mont-Blanc 1.

Fourel, F., Lécuyer, C., Jame, P., Guironnet, A., Boutier, A., Barbier, M., Blamey, N., Brand, U., Fralick, P., 2020. Simultaneous δ2H and δ18O analyses of water inclusions in halite with off-axis integrated cavity output spectroscopy. Journal of Mass Spectrometry 55, e4615. https://doi.org/10.1002/jms.4615

France-Lanord, C., Sheppard, S.M.F., Fort, P.L., 1988. Hydrogen and oxygen isotope variations in the high himalaya peraluminous Manaslu leucogranite: Evidence for heterogeneous sedimentary source. Geochimica et Cosmochimica Acta 52, 513–526. https://doi.org/10.1016/0016-7037(88)90107-X

Gansser, A., 1964. Geology of the Himalayas 308.

Gardien, V., Rabinowicz, M., Vigneresse, J.-L., Dubois, M., Boulvais, P., Martini, R., 2016. Long-lived interaction between hydrothermal and magmatic fluids in the Soultz-sous-Forêts granitic system (Rhine Graben, France). Lithos 246, 110–127.

Garzione, C.N., Dettman, D.L., Quade, J., DeCelles, P.G., Butler, R.F., 2000a. High times on the Tibetan Plateau: Paleoelevation of the Thakkhola graben, Nepal. Geology 28, 339–342.

Garzione, C.N., Quade, J., DeCelles, P.G., English, N.B., 2000b. Predicting paleoelevation of Tibet and the Himalaya from δ18O vs. altitude gradients in meteoric water across the Nepal Himalaya. Earth and Planetary Science Letters 183, 215–229.

Gébelin, A., Jessup, M.J., Teyssier, C., Cosca, M.A., Law, R.D., Brunel, M., Mulch, A., 2017. Infiltration of meteoric water in the South Tibetan Detachment (Mount Everest, Himalaya): When and why? Tectonics 36, 690–713. https://doi.org/10.1002/2016TC004399

Gébelin, A., Mulch, A., Teyssier, C., Jessup, M.J., Law, R.D., Brunel, M., 2013. The Miocene elevation of Mount Everest. Geology 41, 799–802. https://doi.org/10.1130/G34331.1

Giggenbach, W., 1992. Isotopic shifts in waters from geothermal and volcanic systems along convergent plate boundaries and their origin. Earth and planetary science letters 113, 495–510.

Giletti, B.J., Yund, R.A., 1984. Oxygen diffusion in quartz. Journal of Geophysical Research: Solid Earth 89, 4039–4046. https://doi.org/10.1029/JB089iB06p04039

Godin, L., 2003. Structural evolution of the Tethyan sedimentary sequence in the Annapurna area, central Nepal Himalaya. Journal of Asian Earth Sciences 22, 307–328. https://doi.org/10.1016/S1367-9120(03)00066-X

Godin, L., Parrish, R.R., Brown, R.L., Hodges, K.V., 2001. Crustal thickening leading to exhumation of the Himalayan Metamorphic core of central Nepal: Insight from U-Pb Geochronology and 40Ar/39Ar Thermochronology. Tectonics 20, 729–747. https://doi.org/10.1029/2000TC001204

Grabczak, J., Kotarba, M., 1985. Isotopic composition of the thermal waters in the central part of the nepal himalayas. Geothermics 14, 567–575. https://doi.org/10.1016/0375-6505(85)90007-0

Grujic, D., Govin, G., Barrier, L., Bookhagen, B., Coutand, I., Cowan, B., Hren, M.T., Najman, Y., 2018. Formation of a rain shadow: O and H stable isotope records in authigenic clays from the Siwalik Group in eastern Bhutan. Geochemistry, Geophysics, Geosystems 19, 3430–3447.

Grujic, D., Warren, C.J., Wooden, J.L., 2011. Rapid synconvergent exhumation of Miocene-aged lower orogenic crust in the eastern Himalaya. Lithosphere 3, 346–366. https://doi.org/10.1130/L154.1

Harrison, T.M., Célérier, J., Aikman, A.B., Hermann, J., Heizler, M.T., 2009. Diffusion of 40Ar in muscovite. Geochimica et Cosmochimica Acta 73, 1039–1051.

Iaccarino, S., Montomoli, C., Carosi, R., Massonne, H.-J., Langone, A., Visonà, D., 2015. Pressure–temperature–time–deformation path of kyanite-bearing migmatitic paragneiss in the Kali Gandaki valley (Central Nepal): Investigation of Late Eocene–Early Oligocene melting processes. Lithos 231, 103–121.

Jasechko, S., 2019. Global isotope hydrogeology—Review. Reviews of Geophysics 57, 835–965.

Jouzel, J., Merlivat, L., Lorius, C., 1982. Deuterium excess in an East Antarctic ice core suggests higher relative humidity at the oceanic surface during the last glacial maximum. Nature 299, 688–691.

Kawakami, T., Sakai, H., Sato, K., 2019. Syn-metamorphic B-bearing fluid infiltrations deduced from tourmaline in the Main Central Thrust zone, Eastern Nepal Himalayas. Lithos 348, 105175.

Kellett, D.A., Cottle, J.M., Larson, K.P., 2018. The South Tibetan Detachment System: history, advances, definition and future directions. SP 483, 377–400. https://doi.org/10.1144/SP483.2

Kishima, Noriaki., Sakai, Hitoshi., 1980. Oxygen-18 and deuterium determination on single water sample of a few milligrams. Anal. Chem. 52, 356–358.

Kruhl, J.H., Nega, M., 1996. The fractal shape of sutured quartz grain boundaries: application as a geothermometer. Geologische Rundschau 85, 38–43.

Larson, K.P., Ambrose, T.K., Webb, A.A.G., Cottle, J.M., Shrestha, S., 2015. Reconciling Himalayan midcrustal discontinuities: The Main Central thrust system. Earth and Planetary Science Letters 429, 139–146. https://doi.org/10.1016/j.epsl.2015.07.070

Larson, K.P., Godin, L., 2009. Kinematics of the Greater Himalayan sequence, Dhaulagiri Himal: implications for the structural framework of central Nepal. Journal of the Geological Society 166, 25–43.

Leloup, P.H., Liu, Xiaobing, Mahéo, G., Paquette, J.-L., Arnaud, N., Aubray, A., Liu, Xiaohan, 2015. New constraints on the timing of partial melting and deformation along the Nyalam section (central Himalaya): implications for extrusion models. Geological Society, London, Special Publications 412, 131–175. https://doi.org/10.1144/SP412.11

Li, S., Wang, Q., Chen, G., He, P., Ding, K., Chen, Y., Zou, R., 2019. Interseismic Coupling in the Central Nepalese Himalaya: Spatial Correlation with the 2015 Mw 7.9 Gorkha Earthquake. Pure Appl. Geophys. 176, 3893–3911. https://doi.org/10.1007/s00024-019-02121-7

Mattauer, M., 1975. Sur le mecanisme de formation de la schistosite dans l'himalaya. Earth and Planetary Science Letters 28, 144–154. https://doi.org/10.1016/0012-821X(75)90222-8

McCaig, A.M., Wickham, S.M., Taylor, H.P., 1990. Deep fluid circulation in alpine shear zones, Pyrenees, France: field and oxygen isotope studies. Contr. Mineral. and Petrol. 106, 41–60. https://doi.org/10.1007/BF00306407

Menzies, C.D., Teagle, D.A.H., Craw, D., Cox, S.C., Boyce, A.J., Barrie, C.D., Roberts, S., 2014. Incursion of meteoric waters into the ductile regime in an active orogen. Earth and Planetary Science Letters 399, 1–13. https://doi.org/10.1016/j.epsl.2014.04.046

Mulch, A., Chamberlain, C.P., 2007. Stable Isotope Paleoaltimetry in Orogenic Belts The Silicate Record in Surface and Crustal Geological Archives. Reviews in Mineralogy and Geochemistry 66, 89–118. https://doi.org/10.2138/rmg.2007.66.4

Parsons, A., Phillips, R., Lloyd, G., Law, R., Searle, M., Walshaw, R., 2016. Mid-crustal deformation of the Annapurna-Dhaulagiri Himalaya, central Nepal: An atypical example of channel flow during the Himalayan orogeny. Geosphere 12, 985–1015.

Pêcher, A., 1979. Les inclusions fluides des quartz d'exsudation de la zone du M. C. T.

himalayen au Népal central : données sur la phase fluide dans une grande zone de cisaillement crustal. Bulletin de Minéralogie 102, 537–554. https://doi.org/10.3406/bulmi.1979.7302

Pecher, A., 1978. Déformations et métamorphisme associés à une zone de cisaillement. Exemple du grand Chevauchement Central Himalayen (M.C.T.) , transversale des Anapurnas et du Manaslu (Népal) (phdthesis). Université Scientifique et Médicale de Grenoble.

Poage, M.A., Chamberlain, C.P., 2001. Empirical relationships between elevation and the stable isotope composition of precipitation and surface waters; considerations for studies of paleoelevation change. American Journal of Science 1–15.

Putman, A.L., Fiorella, R.P., Bowen, G.J., Cai, Z., 2019. A global perspective on local meteoric water lines: Meta-analytic insight into fundamental controls and practical constraints. Water Resources Research 55, 6896–6910.

Pye, A.E., Hodges, K.V., Keller, C.B., Law, R.D., van Soest, M.C., Bhandari, B., McDonald, C.S., 2022. Prolonged Slip on the South Tibetan Detachment Constrains Tectonic Models for Synorogenic Extension in the Central Himalaya. Tectonics 41, e2022TC007298.

Quade, J., Eiler, J., Daeron, M., Achyuthan, H., 2013. The clumped isotope geothermometer in soil and paleosol carbonate. Geochimica et Cosmochimica Acta 105, 92–107.

Rigaudier, T., Gardien, V., Martineau, F., Reverdy, G., Lécuyer, C., 2012. Hydrogen and Oxygen Isotope Reference Materials for the Analysis of Water Inclusions in Halite. Geostandards and Geoanalytical Research 36, 51–59. https://doi.org/10.1111/j.1751-908X.2011.00139.x

Rossi, M., Rolland, Y., 2014. Stable isotope and Ar/Ar evidence of prolonged multiscale fluid flow during exhumation of orogenic crust: Example from the Mont Blanc and Aar Massifs (NW Alps): Multi-scale fluid flow in the Alps. Tectonics 33, 1681–1709. https://doi.org/10.1002/2013TC003438

Rowley, D.B., Pierrehumbert, R.T., Currie, B.S., 2001. A new approach to stable isotope-based paleoaltimetry: implications for paleoaltimetry and paleohypsometry of the High Himalaya since the Late Miocene. Earth and Planetary Science Letters 188, 253–268. https://doi.org/10.1016/S0012-821X(01)00324-7

Sauniac, S., Touret, J., 1983. Petrology and fluid inclusions of a quartz-kyanite segregation in the main thrust zone of the Himalayas. Lithos 16, 35–45. https://doi.org/10.1016/0024-4937(83)90032-4

Taillefer, A., Guillou-Frottier, L., Soliva, R., Magri, F., Lopez, S., Courrioux, G., Millot, R., Ladouche, B., Le Goff, E., 2018. Topographic and Faults Control of Hydrothermal Circulation Along Dormant Faults in an Orogen. Geochemistry, Geophysics, Geosystems 19, 4972–4995. https://doi.org/10.1029/2018GC007965

Van den Kerkhof, A.M., Hein, U.F., 2001. Fluid inclusion petrography. Lithos, Fluid Inclusions: Phase Relationships - Methods - Applications. A Special Issue in honour of Jacques Touret 55, 27–47. https://doi.org/10.1016/S0024-4937(00)00037-2

Vannay, J.-C., Hodges, K.V., 1996. Tectonometamorphic evolution of the Himalayan metamorphic core between the Annapurna and Dhaulagiri, central Nepal. Journal of Metamorphic Geology 14, 635–656. https://doi.org/10.1046/j.1525-1314.1996.00426.x

Webb, A.A.G., Yin, A., Harrison, T.M., Célérier, J., Burgess, W.P., 2007. The leading edge of the Greater Himalayan Crystalline complex revealed in the NW Indian Himalaya: Implications for the evolution of the Himalayan orogen. Geol 35, 955. https://doi.org/10.1130/G23931A.1

Yin, A., Dubey, C.S., Kelty, T.K., Gehrels, G.E., Chou, C.Y., Grove, M., Lovera, O., 2006.

Structural evolution of the Arunachal Himalaya and implications for asymmetric development of the Himalayan orogen. Current Science 90, 195–206.

Zhao, W., Nelson, K.D., Che, J., Quo, J., Lu, D., Wu, C., Liu, X., 1993. Deep seismic reflection evidence for continental underthrusting beneath southern Tibet. Nature 366, 557–559. https://doi.org/10.1038/366557a0

Author Contributions R.M., G.M. and V.G., conceived the project. R.M., G.M., and B.B., collected the Kali Gandaki samples and A.P., collected Mansalu samples. R.M., prepared the samples, performed the extraction process of fluid inclusions. R.M., E.B and P.J., performed the stable isotopic analyses. R.M wrote the manuscript with contributions from all authors.

Declaration of competing interest

The authors declare that they have no known competing financial interests or personal relationships that could have appeared to influence the work reported in this paper.

Acknowledgments We thank the University of Kathmandu and especially Ananta Gajurel and the Earth Paradise team Bhim Chand, Tej Bikram Shahi and driver Man Bahadur Salami Magar for field organization and assistance. This work was supported by the Laboratoire de Geologie de Lyon: Terre, Planètes, Environnement, the Doctoral School PHAST (Univ. Lyon 1) , V. Gardien CNRS ISOTOP2020 and G. mahéo INSU TelluS Syster programs. This manuscript benefits from constructive comments by Djordje Grujic and an anonymous reviewer.

Appendix A. Supplementary material

Supplementary material related to this article can be found online at https://doi .org /10 .1016 /j .epsl .2023 .11818